Hidden diversity of vacancy networks in Prussian blue analogues

Arkadiy Simonov[1,2], **Trees De Baerdemaeker**[1,3], **Hanna L. B. Boström**[1,4], **María Laura Ríos Gómez**[5,6], **Harry J. Gray**[1], **Dmitry Chernyshov**[7], **Alexey Bosak**[8], **Hans-Beat Bürgi**[9,10], **Andrew L. Goodwin**[1,*]

[1]Inorganic Chemistry Laboratory, Department of Chemistry, University of Oxford, Oxford, U.K.
[2]Laboratory for Multifunctional Ferroic Materials, Department of Materials, ETH Zürich, Zürich, Switzerland [3]Centre for Surface Chemistry and Catalysis, KU Leuven, Leuven, Belgium [4]Department of Chemistry, Uppsala University, Uppsala, Sweden [5]Departamento de Polímeros, Instituto de Investigaciones en Materiales, Universidad Nacional Autónoma de México, Ciudad de México, Mexico [6]Department of Materials Science and Metallurgy, University of Cambridge, Cambridge, U.K. [7]Swiss-Norwegian Beam Lines at the European Synchrotron Radiation Facility, Grenoble, France [8]European Synchrotron Radiation Facility, Grenoble Cedex, France [9]Department of Chemistry, University of Zürich, Zürich, Switzerland [10]Department of Chemistry and Biochemistry, University of Berne, Bern, Switzerland

Abstract

Prussian blue analogues (PBAs) are a diverse family of microporous inorganic solids, famous for their gas storage,[1] metal-ion immobilization,[2] proton conduction,[3] and stimuli-dependent magnetic,[4,5] electronic,[6] and optical[7] properties. The family includes the double-metal cyanide (DMC) catalysts[8,9] and the hexacyanoferrate/hexacyanomanganate (HCF/HCM) battery materials.[10,11] Central to the various physical properties of PBAs is the ability to transport mass reversibly, a process enabled by structural vacancies. Normally presumed random,[12,13] vacancy arrangements are crucial because they control micropore network characteristics, and hence diffusivity and

adsorption profiles.[14,15] The long-standing obstacle to characterising PBA vacancy networks is the inaccessibility of single crystals.[16] Here we report the growth of single crystals of a range of PBAs. By measuring and interpreting their X-ray diffuse scattering patterns, we identify a striking diversity of non-random vacancy arrangements that is hidden from conventional crystallographic analysis of powders. Moreover, we rationalise this unexpected phase complexity in terms of a simple microscopic model based on local rules of electroneutrality and centrosymmetry. The hidden phase boundaries that emerge demarcate vacancy-network polymorphs with profoundly different micropore characteristics. Our results establish a foundation for correlated defect engineering in PBAs as a means of controlling storage capacity, anisotropy, and transport efficiency.

The true crystal structures of PBAs—as of Prussian blue itself—have long posed a difficult and important problem in solid-state chemistry because their ostensibly simple powder diffraction patterns [Figure 1a] belie a remarkable complexity at the atomic scale.[17,18,19] The common parent structure is based on the cubic lattice and corresponds to the idealised composition $M[M'(CN)_6]$. Atoms of type M and M' (usually transition-metal cations) occupy alternate lattice vertices and are octahedrally coordinated by bridging cyanide ions (CN^-) at the lattice edges [Figure 1b]. There is a close parallel to the double perovskite structure; indeed the considerations of covalency and octahedral coordination that stabilise perovskites amongst oxide ceramics also favour this same architecture for transition-metal cyanides, accounting for the chemical diversity of PBAs.[20] Charge balance requires that the formal oxidation states of M and M' sum to six, as in $Cd^{II}[Pd^{IV}(CN)_6]$.[21]

Prussian blue itself is a mixed-valence cyanide of iron in its 2+ and 3+ oxidation states,[22,23] and so its composition cannot respect this oxidation-state-sum rule. Instead the rule is circumvented by vacancies: the composition is well approximated by the formula $Fe^{III}[Fe^{II}(CN)_6]_{3/4} \bullet_{1/4} \bullet xH_2O$, where the symbol • represents a $[Fe^{II}(CN)_6]^{4-}$ vacancy.[18] Vacancies are usually filled by water molecules, which complete the coordination sphere of the M cation;[12] we use the term 'vacancy' to encompass the possible occupancy of the M'-site with water. Each vacancy gives rise to a micropore of effective diameter ~8.5 Å that exceeds the distance between neighbouring M'-sites ($a/2 \approx 7.2$ Å).[24] Hence a pair of neighbouring vacancies, if present, connects to form a larger micropore.[1] A random vacancy distribution would imply bulk microporosity, since the vacancy fraction exceeds the percolation threshold for the face-centered cubic (FCC) M' sublattice (~0.20).[25] But Prussian Blue is not microporous: single-crystal X-ray diffraction has shown that vacancies tend to avoid one another by adopting a specific ordered arrangement [Figure 1b].[18] A vacancy fraction of ¼ is the greatest that can support complete vacancy isolation.

PBAs with a nominal composition of $M^{II}[M'^{III}(CN)_6]_{2/3} \bullet_{1/3} \bullet xH_2O$ (hereafter "M[M']") contain an even higher fraction of M'-site vacancies.[12,20,26] Hence geometry dictates that these vacancies—whatever their distribution—must form connected neighbour-pairs [Figure 1b]. The existence and nature of any extended micropore network that then develops depends on longer-range vacancy correlations. The collective micropore structure of PBAs is remarkably poorly understood, despite the relevance of mass transport to the many important properties of the family.[1,11] So what *is* known? Adsorption isotherm measurements reflect a

diversity of pore characteristics across PBAs.[26,27] Solid-state [113]Cd NMR measurements have evidenced non-statistical vacancy distributions in Cd[Fe$_x$Co$_{1-x}$].[28] Weak primitive superlattice reflections have sometimes been observed and sometimes not in powder X-ray diffraction (PXRD) patterns; their presence has usually been interpreted as evidence for (partial) Prussian-blue-type vacancy order.[16] High-resolution transmission electron microscopy has revealed vacancy chains in some Cu-PBAs and their absence in other Zn-containing samples.[29] And in the only existing single-crystal diffraction study of a PBA (*viz.* Mn[Mn]), structured diffuse scattering was observed and interpreted in terms of Warren–Cowley correlation parameters.[30,31] Taken together, these observations suggest that (i) vacancy distributions are unlikely to be random, and (ii) there must be substantial variability in the pore networks of different PBAs.

In this study, we have characterised vacancy correlations in a range of PBAs by growing single crystals, measuring their X-ray diffuse scattering patterns, and interpreting these patterns *via* three-dimensional difference pair distribution function (3D- PDF) analysis and Monte Carlo (MC) simulations.

For every crystal we investigated, the corresponding X-ray diffraction pattern contained weak but highly-structured diffuse scattering, which is the hallmark of strongly-correlated disorder.[32] Representative (*hk*0) cuts of our diffuse scattering patterns are shown for a selection of PBAs in Figure 2, where we include the only other single-crystal diffuse scattering pattern ever reported for a PBA—namely for Mn[Mn].[30,31] Inverse Fourier transform of the normalised diffuse scattering function yields the 3D- PDF.[33] The form of all our 3D- PDFs is well-described by a convolution of the contribution from an individual $[M'^{III}(CN)_6]^{3-}$ anion together with an occupational correlation function. Hence the diffuse scattering we observe arises from correlations in $[M'^{III}(CN)_6]^{3-}$ occupancy rather than any alkali cation or solvent inclusion. The scattering is also predominantly elastic, since the 3D- PDF is dominated by occupational correlations and not the signature of cooperative displacements. In PXRD measurements, orientational averaging conceals the diffuse scattering within the background and/or to causes it to resemble primitive superlattice reflections;[31] it is in this sense that the vacancy correlations from which the diffuse scattering arises are "hidden".

We find a surprising diversity of diffuse scattering patterns amongst different PBAs. This is true even for crystals with the same nominal composition but grown separately (the example in Figure 2 is a pair of Mn[Co] crystals grown in different media). So our experimental data unambiguously show that the vacancies in PBAs are distributed in a highly non-random manner, and that these distributions can be fundamentally different for different samples.

How might we understand this diversity, and what are its implications for mass transport in PBAs? To answer these questions we have developed a very simple vacancy interaction model that is nevertheless capable of rationalising the various experimental diffuse scattering patterns. MC simulations driven by this set of interactions generate representative pore network configurations for each phase that can then be used to determine physical properties of relevance to mass transport and storage. Our model contains just two ingredients, each based on simple crystal-chemical considerations. The first favours a uniform vacancy

distribution—*i.e.* such that for each M-site four of its six neighbouring M′-sites are occupied and two are vacant. This contribution reflects Pauling's "electroneutrality" principle.[34] The second ingredient favours locally-centrosymmetric arrangements, which we expect to be more or less important depending on M-site chemistry.

Formally, we represent the MC energy by

$$E = \sum_{\mathbf{r} \in \{M\}} \left[J_1 \left(4 - \sum_{\mathbf{r}' \in \frac{1}{2}\langle 100 \rangle} e_{\mathbf{r}+\mathbf{r}'} \right)^2 + \frac{J_2}{2} \sum_{\mathbf{r}' \in \frac{1}{2}\langle 100 \rangle} \left(e_{\mathbf{r}+\mathbf{r}'} - e_{\mathbf{r}-\mathbf{r}'} \right)^2 \right], \quad (1)$$

where the sum is taken over all M-sites at positions $\mathbf{r}$, with the neighbouring M′-site states $e_{\mathbf{r}\pm\mathbf{r}'} = 0$ (vacant) or 1 (present), and $J_1, J_2 > 0$ quantifying the strength of the electroneutrality and centrosymmetry terms, respectively. The occupancy fraction $\langle e \rangle = \frac{2}{3}$. The quadratic form of the electroneutrality component comes from the leading term in the series expansion in local charge at the M-site. We performed MC simulations for a range of $J' = J_1/J_2$ ratios and effective temperatures $T' = T/J_2$. Our results are shown in Figure 3a, represented in terms of the single-crystal X-ray diffuse scattering patterns calculated from an ensemble of 40 MC configurations for each point across an evenly-distributed mesh of J', $\log(T')$.

The phase behaviour given by this simple MC model is remarkable for a number of reasons. Clearly the form of the diffuse scattering—and, as we will come to see, of the vacancy-network topology—is an extremely sensitive function of J' and T'. This observation mirrors our experimental results: namely, that small variations in synthesis conditions or PBA composition strongly affect the diffuse scattering. Such sensitivity arises because the two interaction terms of electroneutrality and centrosymmetry operate in tension: they are resolvable when the vacancy fraction is ¼ (giving the ordered Prussian blue vacancy arrangement shown in Figure 1b; *cf* sample I in Ref. 18), but become frustrated as the vacancy fraction increases. Hence the crystal-chemical considerations embedded in Eq. (1) drive an unexpectedly complex configurational landscape for the $\frac{1}{3}$ M′-site vacancy fraction of PBAs. We note the parallel to geometric frustration in relaxor ferroelectrics (*e.g.* $Pb(Mg_{1/3}Nb_{2/3})O_3$) and relaxor ferromagnets (*e.g.* $La(Sb_{1/3}Ni_{2/3})O_3$), where the problem of 1:2 decoration of the FCC lattice is also central.[35,36]

The experimental diffuse scattering patterns given in Figure 2 are well approximated by our MC simulations at different values of J' and T' [Figure 3a,b]. The implication is that electroneutrality and centrosymmetry are alone sufficient to account for the basic form and diversity of diffuse scattering patterns observed experimentally.

But what determines J' and T' for a given system? PBAs with Jahn-Teller-active M-site cations (Cu[Co]) correspond to smaller values of J', which is sensible because crystal field effects[20] must increase the relative importance of the J_2 term. By contrast, crystal-field-inactive M-site cations correspond to larger J'; the larger values for Zn[Co] and Cd[Co] likely reflect the empirical propensity of Zn and Cd to adopt acentric coordination geometries in their pseudobinary cyanides[37,38] and rhombohedral PBAs[39] [Figure 3c]. So PBA composition controls J', with M-site chemistry more important than that of the M′-site.

Solid solutions will likely span the range of J' values bounded by the corresponding endmembers, which in the case of Cu/Zn mixtures renders most of J'-space accessible synthetically. The effective MC temperature T' appears not to be driven by composition but reflects instead precursor concentration and crystal growth rate (high $T' \equiv$ rapid precipitation and/or high oversaturation). Our different Mn[Co]($'$) samples are associated with similar J' but different T', with the lower T' value for the slower-grown sample (gel diffusion). By reducing synthesis temperature and/or precursor concentrations, it may prove possible to access log T' values lower than those we report here. So, from a synthetic viewpoint, there is genuine scope for navigating much of J', T'-space through judicious choice of PBA chemistry (J') and synthesis approach (T').

Just as the calculated diffuse scattering patterns are unexpectedly diverse for our MC configurations, so too are the corresponding vacancy-network structures. Despite their considerable disorder, these networks have meaningfully different physical characteristics that we discuss in greater detail below. At the simplest level, different configurations have vacancy networks with different coordination number and geometry distributions [Figure 4 and Extended Data Figure 1]. Low values of J' give networks dominated by square-planar nodes; at large J', one finds low-dimensional motifs based on 120° zig-zag chains instead. High T' favours a greater diversity of network geometries and low effective temperatures stabilise uniform vacancy networks and/or phase segregation.

Collectively, the various different scattering patterns and micropore geometries identify previously-unknown phase domains of distinct vacancy-network polymorphs, the boundaries between which are essentially hidden from conventional PXRD analysis [Figure 3b]. These boundaries emerge from our MC analysis either from anomalies in the MC energy gradient $\frac{\Delta E}{\Delta T}$, or by variation in anisotropy. The I/III, I/V and II/III transitions are examples of the former; III/IV and IV/V are examples of the latter. Despite the differences in diffuse scattering patterns (and pore network characteristics) throughout phase I, the entire phase field can be navigated without any discontinuity in energy or its derivative, or in anisotropy. Phase II is actually a physical mixture of separate components with ¼ and ½ vacancy fractions: one has the Prussian Blue structure, and the other is layered with tetragonal symmetry. Given this admixture, we don't expect the phase to be relevant to PBA chemistry. Phase V is also tetragonal, but is heavily disordered and may well be relevant to PBAs. Phase IV represents a competing mixture of (isotropic) III and (anisotropic) V components, and includes a morphotropic phase boundary. Phase VI contains a tetragonally-ordered array of zig-zag pores. Our confidence in the detail of the phase diagram between phases I and VI is reduced by the difficulty of MC equilibration at such low T' values.

In Figure 3d we show a range of physical quantities calculated from our MC configurations as a function of J' and T'. Some of these—*e.g.* the MC energy gradient $\log\left(\frac{\Delta E}{\Delta T}\right)$ or the diffuse scattering localization $L = \log\left[\frac{\sum I^2}{(\sum I)^2}\right]$—serve primarily to highlight phase boundaries, but others are particularly relevant to the transport properties of PBA phases. For example, tortuosity τ is a measure of the curvature of internal pore space.[40] It affects the rate of mass transport (*i.e.* conductance):[41]

$$C \propto \frac{\rho}{\tau^2}, \tag{2}$$

where ρ is the number of vacancy neighbour-pairs per formula unit.[42] We find C varies by a factor of two within the high-temperature disordered phase I and by yet another factor of two on progressing into lower-temperature phases. Even accessible pore volumes vary substantially: we calculate differences $> 25\%$ for this same family of configurations. Moreover, in the anisotropic phases II, V, and VI, transport depends on orientation.

This unexpected variability in micropore characteristics helps explain the irreproducibility and diversity of sorption and storage properties observed experimentally. But it also highlights the opportunity for property optimisation *via* synthetic control over vacancy correlations—*i.e.* defect engineering.[43] For example, the value of C should be maximised for battery materials, which might be achieved by combining low J' (*e.g.* M = Cu^{2+}) and high T' (rapid precipitation). This analysis is remarkably consistent with the empirical identification of polycrystalline Cu[Fe] ("CuHCF") as a high-performance battery material.[10]

Our results identify many future challenges. We have focussed on single-crystal samples because of the relative insensitivity of PXRD to the vacancy polymorphism of this family. So establishing a robust link between vacancy correlations and (*e.g.*) ion-storage capacity in HCFs will require innovative approaches to measuring and interpreting diffuse scattering from microcrystalline samples. Serial femtosecond crystallography[44] and/or electron diffraction[45] may help. With access to vacancy-network models, it is possible that powder PDF measurements may now allow some experimental sensitivity, *e.g.* as flagged in Ref. 46. Our analysis has also been intentionally simplistic: we have not needed to invoke the role of alkali-metal inclusion, nor have we considered M´ chemistry or cooperative JT effects.[47] Yet these additional degrees of freedom must allow further chemical control over pore network characteristics. An obvious opportunity is to extend the phase fields of Figure 3a as a function of alkali cation concentration; one might anticipate simpler behavior as the vacancy fraction reduces. There are many variables one might exploit in tailoring PBA network structures—*e.g.* concentration, pH, crystal growth rate and media, temperature, speciation, solubility, competing ions, chelation—and establishing rules that link these variables to vacancy polymorphs represents an enormous challenge. Vacancy-network polymorphism may affect magnetic order, spin-state transitions, orbital order, and photophysics. Moreover, any mechanistic understanding of DMC catalysis will require characterisation of particle surface structure, which may be substantially more complex than previously anticipated. And, stepping back, one might ask whether a similar hidden polymorphism plays a role in other microporous phases, such as metal–organic frameworks[48] or zeolites.[49]

Methods

Single crystal growth

Single-crystal PBA samples were in all but one case grown using slow-diffusion methodologies. The exception was the crystal of Mn[Mn], for which we used the same

sample reported in Ref. 31. All other samples were prepared by counterdiffusion of aqueous solutions of a potassium hexacyanometallate(III) and a divalent transition-metal nitrate, chloride, sulfate, or acetate. Precursor salts were used as supplied and without further purification; the identity and quantity of these salts are summarised in Extended Data Table 1. Crystals of Cd[Co], Mn[Co]´, Mn[Fe], and Zn[Co] were grown in H-cells, while those of Mn[Co], Cu[Co], and Co[Co] were grown from silica gel. For H-cell diffusion reactions, aqueous solutions of precursor salts (0.5 mL) were placed in opposite arms of a glass H-cell. The cell was then filled with water, taking care not to disturb the solution–water interface. The H-cell was sealed and left undisturbed. Crystal growth was typically completed within 1–3 weeks. For gel-diffusion reactions, a transition-metal-impregnated gel was first prepared. Aqueous solutions of Na_2SiO_3 (2 M, 2.5 mL), M^{2+} salt (0.01–0.15 M, 2.5 mL), and acetic acid (2 M, 5 mL) were combined in a 15 mL centrifuge tube. The gel was allowed to set overnight. An approximately stoichiometric quantity of $K_3[M´(CN)_6]$ was then dissolved in water (2.5 mL), and the corresponding solution layered carefully above the gel. The tube was sealed and the system left undisturbed. Crystal growth was typically completed within 3–7 days, with the first crystals appearing within 24 h. In all cases, care was taken not to dehydrate our samples.

Single crystal diffuse scattering

Single crystal diffuse scattering measurements were carried out using the I19 beamline at the Diamond Light Source (U.K.) and the BM01 beamline at the European Synchrotron Radiation Facility (France). Both beamlines are equipped with Pilatus 2M area pixel-counting detectors. The same data acquisition strategy was used at both beamlines and consisted of a single 360° rotation scan around the omega axis. The key experimental parameters are summarised in Extended Data Table 2.

Crystal orientation determination, and Bragg peaks indexing and integration were carried out using the package xds.[51] Reconstruction of 3D diffuse scattering was performed using the program meerkat.[52] Air scattering was measured on an empty instrument, reconstructed in the same way as the signal and then subtracted from the signal. The diffuse scattering data so obtained were then averaged in the $m\bar{3}m$ Laue group. The reconstruction of the Mn[Mn] dataset from Ref. 31 followed exactly the same procedure, using the original data frames.

Preparation of diffuse scattering inset images

The single-crystal X-ray diffuse scattering patterns shown in the insets of Figure 2 were prepared from the three-dimensional scattering reconstruction using the projection method of Ref. 53. First, the $hk0$ section of each dataset was extracted, then the Bragg peaks were cut away, along with all surrounding thermal diffuse scattering. Next, the diffuse scattering was projected onto a single Brillouin zone. For this projection, square diffuse scattering patches with the diagonal corners (h,k) and $(h+2,k+2)$ with $h = 2n$, $k = 2m$ were taken and summed together. In the case of binary disorder, this procedure allows removal of the contribution of the molecular form factor from the diffuse scattering. The resulting projection contains information only regarding the distribution of defects and does not include information of the chemical composition of those defects.[53] This process is what

allows direct comparison to simulated diffuse scattering patches calculated from Monte Carlo configurations.

3D- PDF analysis

Diffuse scattering was analysed using the 3D- PDF method.[33,54] The experimental diffuse scattering was reconstructed as stated above, the background air scattering subtracted by using an empty instrument run, and an optimal scale coefficient selected manually. The resulting diffuse scattering was averaged in the $m\overline{3}m$ Laue group using outlier rejection as described by Blessing.[55] Bragg peaks were removed using the "punch and fill" procedure:[56] spheres of intensity around the Bragg peaks were removed to ensure omission of thermal diffuse scattering contributions from subsequent analysis. The resulting holes were filled with the median intensity from a small surrounding region of reciprocal space. Since the crystals showed a large amount of thermal diffuse scattering around the Bragg peaks, the radius of spheres for punching and filling was chosen to be relatively large—approximately 0.5 reciprocal lattice units. Finally, the 3D- PDF map was calculated using fast Fourier transform. Quantitative 3D- PDF refinement was carried out using the program YELL.[57]

Here we give details for the representative case of the Co[Co] sample. The diffuse scattering map is presented in Extended Data Figure 2a. Note that, due to over-correction of the background, some pixels show negative intensities (marked red).

The 3D- PDF map is presented in Extended Data Figure 2b. The 3D- PDF map gives the difference between the crystal pair distribution function and its Patterson function. This map should be interpreted in an analogous manner to the Patterson map: in particular, the signal at a position uvw corresponds to all the pairs of atoms in the structure which are separated by the vector components $u = x_i - x_j$, $v = y_i - y_j$, $w = z_i - z_j$, where i and j index atom pairs. The 3D- PDF consists of positive and negative signals. Positive signals mean that corresponding interatomic pairs are present more often in the real structure than in the average structure; negative signals mean the opposite. For a more detailed introduction to the 3D- PDF see Ref. 33.

Interpretation of the 3D- PDF map in the current case is simplified by the presence of the high-Z atom cobalt in the partially-vacant $[Co(CN)_6]^{3-}$ moiety. Since the contribution of each interatomic pair is proportional to the product of the number of electrons in both atoms, the 3D- PDF will be dominated by signals from pairs containing Co atoms. All atoms which are more likely to appear together with cobalt will give a positive contribution, and all of the atoms which tend to appear less often will be seen as negative signals.

The centre of the 3D- PDF space is positive and represents all interatomic vectors within the $[Co(CN)_6]^{3-}$ group. In the $uv0$ section, the signal appears as a cross. This is because the heavy Co atom is in the centre, and the four equatorial CN^- groups are around it. Similar crosses are located at positions corresponding to the face centered lattice vectors. They correspond to the correlation between simultaneously-present $[Co(CN)_6]^{3-}$ groups. By contrast, the nearest neighbour at 0.5,0.5,0 shows a negative correlation, meaning that the probability of finding two $[Co(CN)_6]^{3-}$ groups separated by this vector is less than 4/9 (the fraction observed in a completely random distribution of vacancies).

The program YELL allows refinement of the 3D- PDF in terms of pair correlations. In order to speed up the refinement, the voxel size of diffuse scattering was increased in reciprocal space by binning sets of $5 \times 5 \times 5$ voxels together. The final voxel resolution was 1/6 reciprocal lattice units, corresponding to the PDF map containing correlations spanning the nearest 3 unit cells in x, y and z directions.

In our modelling of the 3D- PDF, we have assumed that 2/3 of the M'-sites are occupied by $[Co(CN)_6]^{3-}$ ions and the remaining 1/3 are occupied by an H_2O-filled vacancy [Extended Data Figure 3]. The latter was modelled with six structural water molecules, and four zeolitic water molecules. The model 3D- PDF is shown in the right-hand panel of Extended Data Figure 2b. It is clear that the model accounts well for the majority of the observed features. The resulting correlation coefficients for the first 44 neighbours are listed in Extended Data Table 3.

Monte Carlo simulations and analysis

Monte Carlo (MC) simulations were carried out using a parallel tempering approach[58] implemented within custom-written code. We note for context the use elsewhere of MC methods for interpreting single-crystal diffuse scattering.[32,58b] In our case, for each J' value, an ensemble of 129 configurations was generated and MC simulations carried out at a suitable distribution of temperatures T' ($1.5 < T' < 9.94658$ with $T'_i = 1.014889 \times T'_{i-1}$; *i.e.* evenly spread in log T'). Each configuration represented a $12 \times 12 \times 12$ supercell of the FCC unit-cell, containing a total of 6912 sites. Configurations were initialised with a random distribution of vacancies, such that exactly 1/3 of the sites were vacant in total. Monte Carlo steps involved swap moves: two sites, one occupied and one vacant, were selected at random and their contents swapped. In addition to these Monte Carlo steps, the algorithm involved replica exchange. An attempt for one replica exchange was performed every four Monte Carlo steps. For this, two reservoirs with nearest temperatures were selected at random, and the temperature swap was performed with the probability $p = \exp\left[(E_1 - E_2)/\left(T_1^{-1} - T_2^{-1}\right)\right]$.

The configurations were equilibrated for 100 epochs (one epoch corresponds to the number of steps required to visit each site twice on average), following production steps of 80 epochs each. The thermodynamic quantities ($\langle E \rangle, \langle E^2 \rangle$) were sampled each MC step, while all other quantities (tortuosity, diffuse scattering, *etc.*) were calculated from 40 configurations separated from one other by two epochs. Convergence was determined by the convergence of the MC energies of the models. It was found that almost all configurations were converged except for a few configurations of polymorphs II, IV, and VI at the very lowest sampled temperatures. The diffuse scattering from unconverged configurations of phase IV, however, showed sharp streaks along $\mathbf{a}$*, $\mathbf{b}$*, and $\mathbf{c}$* which are very similar to the streaks observed experimentally in Mn[Co]. Since in our view the experimental crystals are also not necessarily all at thermodynamic equilibrium, we decided to keep the simulation without change. The diffuse scattering patterns shown in Figure 3 were calculated using the Fast Fourier Transform, averaged in the $m\overline{3}m$ Laue group. Only the hk0 planes were extracted and shown.

Surface area and accessible pore volume calculations were calculated using the ZEO++ code[60] for small configurations, and a related custom-written code for larger configurations.

Tortuosity was calculated as the average of the distance from a vacancy site to a plane along the percolation channel divided by the 'flight' distance to the plane: $\tau = \langle d_i/d_i^a \rangle$. Here, d_i is the length along the percolating links from the vacancy to a plane and d_i^a is the 'flight' distance of the same vacancy to the plane. The values of tortuosity were calculated in the **a**, **b**, and **c** directions and then averaged. Since vacancies are connected with each other in $\langle 110 \rangle$ directions, the smallest tortuosity achievable in this structure is 2.

Since strain effects mean the energy of charged defects may not always scale as the square of the charge (see, for instance, Ref. 61) we have checked the robustness of our results with the modified Hamiltonian

$$E = \sum_{\mathbf{r} \in \{M\}} \left[J_1 \left| 4 - \sum_{\mathbf{r'} \in \frac{1}{2}\langle 100 \rangle} e_{\mathbf{r}+\mathbf{r'}} \right| + \frac{J_2}{2} \sum_{\mathbf{r'} \in \frac{1}{2}\langle 100 \rangle} (e_{\mathbf{r}+\mathbf{r'}} - e_{\mathbf{r}-\mathbf{r'}})^2 \right], \quad (2)$$

where, compared to (1), we have used the absolute value in the J_1 term. The resulting phase diagram is essentially the same, albeit the simulations converge significantly slower due to additional frustration in the phase V. The diffuse scattering from this model is shown in Extended Data Figure 4.

Surface area and accessible pore volume calculations were performed using the ZEO++ code. [60] We found the code to be prohibitively slow for the large $12 \times 12 \times 12$ configurations, and so we used smaller configurations ($6 \times 6 \times 6$) for initial calculations. In these calculations we observed that both accessible volume and accessible surface areas were directly proportional to the number of accessible vacancies in the structure. Consequently, for the larger $12 \times 12 \times 12$ configurations, we obtained the final values using the following relations: $S_a = 1551 N_a/N_t$ [m^2/g] and $V_a = 0.074 N_a/N_t$ [ml/g]. Here, V_a is the total accessible volume, S_a is the accessible surface, N_a is the number of accessible vacancies and N_t is the total number of vacancies in the simulation box.

Location of projections within the phase diagram

For all but one PBA system, the corresponding experimental diffuse scattering 'tiles' shown in Figs. 3 of the main text were positioned in order to minimise the difference between experimental and model intensities. We determined these differences using the diffuse scattering R-factor:

$$R = \frac{\sum_{hkl} \left\{ I_e(hkl) - [s I_m(hkl) + c] \right\}^2}{\sum_{hkl} [I_e(hkl)]^2}. \quad (3)$$

Here, s is the scale coefficient of the model, c a constant background, and I_e, I_m the experimental and model scattering intensities, respectively. The parameters s and c were determined by linear minimisation of the R-factor.

The exception to this approach was for the case of Mn[Co]. Here, our experimental data showed the presence of sharp streaks of diffuse scattering parallel to the **a***, **b***, and **c*** directions. The R-factor approach described above could not correctly place this tile due to

the absence of accurate modelling of the experimental resolution function. Instead, this particular tile was placed within the area IV of the phase diagram, which we felt best accounted for the qualitative features of the experimental data. The projected experimental diffuse scattering patterns and the closest matching tiles from the model phase diagram are compared in Extended Data Figure 5.

As a final point we note that comparison metrics alternative to the one we propose here are easily envisaged. We tested a number during the course of our own analysis and found that different approaches gave slightly different positions for the various diffuse scattering tiles. Nevertheless, in essentially all cases the general features noted in the main text were preserved; *e.g.* that Zn[Co] and Cd[Co] were placed on the right-hand side of the phase diagram, Cu[Co] on the left, and the M = Mn,Co samples near $J' = 1$.

Additional diffraction features in PBAs

In addition to the vacancy-driven diffuse scattering and satellites described in the main text, we observed some diffraction features that are not related to vacancy order. These intensities are not covered by our model (understandably), but we expand here on why their presence does not affect our analysis or the conclusions drawn.

For the Cu[Co] sample, we observed not only vacancy-driven diffuse scattering and Bragg peaks corresponding to P centering, but also additional Bragg peaks near the half-integer positions. The indices of such reflections are approximately equal to $(h, k, 0.9l + 0.5)$; *i.e.* they come from a tetragonally-distorted crystallite with parameter $a' = a_{main}$, $c' = 1.1 a_{main}$ [Extended Data Figure 6]. Since other Bragg peaks from this sample showed no signs of such tetragonal distortion, and the total intensity of additional reflections was less than 1% of the total main reflections, we can conclude that these additional reflections come from a tetragonally-distorted impurity precipitate which is coherent with respect to the primary cubic matrix.

Some crystals also showed diffuse scattering centred at positions of the type $(h + 1/3, k + 1/3, l)$ [Extended Data Figure 7]. In particular these additional signals were visible for Cd[Co], Mn[Mn], Mn[Fe], Mn[Co]′ crystals, but not for Mn[Co], Zn[Co], Cu[Co] or Co[Co] crystals. The intensity of this diffuse scattering was zero for $l = 0$ (in the planes passing through the center of reciprocal space), and increased with the magnitude of l. This is a typical signature of diffuse scattering from displacive correlations, with displacement polarised along the **c** direction. Interestingly, in the Mn[Co]′ and Cd[Co] samples the diffuse scattering intensities follow tetragonal symmetry, rather than cubic symmetry of the Bragg peaks. Note that since displacive diffuse scattering is absent in the $hk0$, $h0l$ and $0kl$ sections it has no contribution to the projected diffuse scattering tiles from Figs. 2 and 3 and thus does not influence the analysis of vacancy distributions.
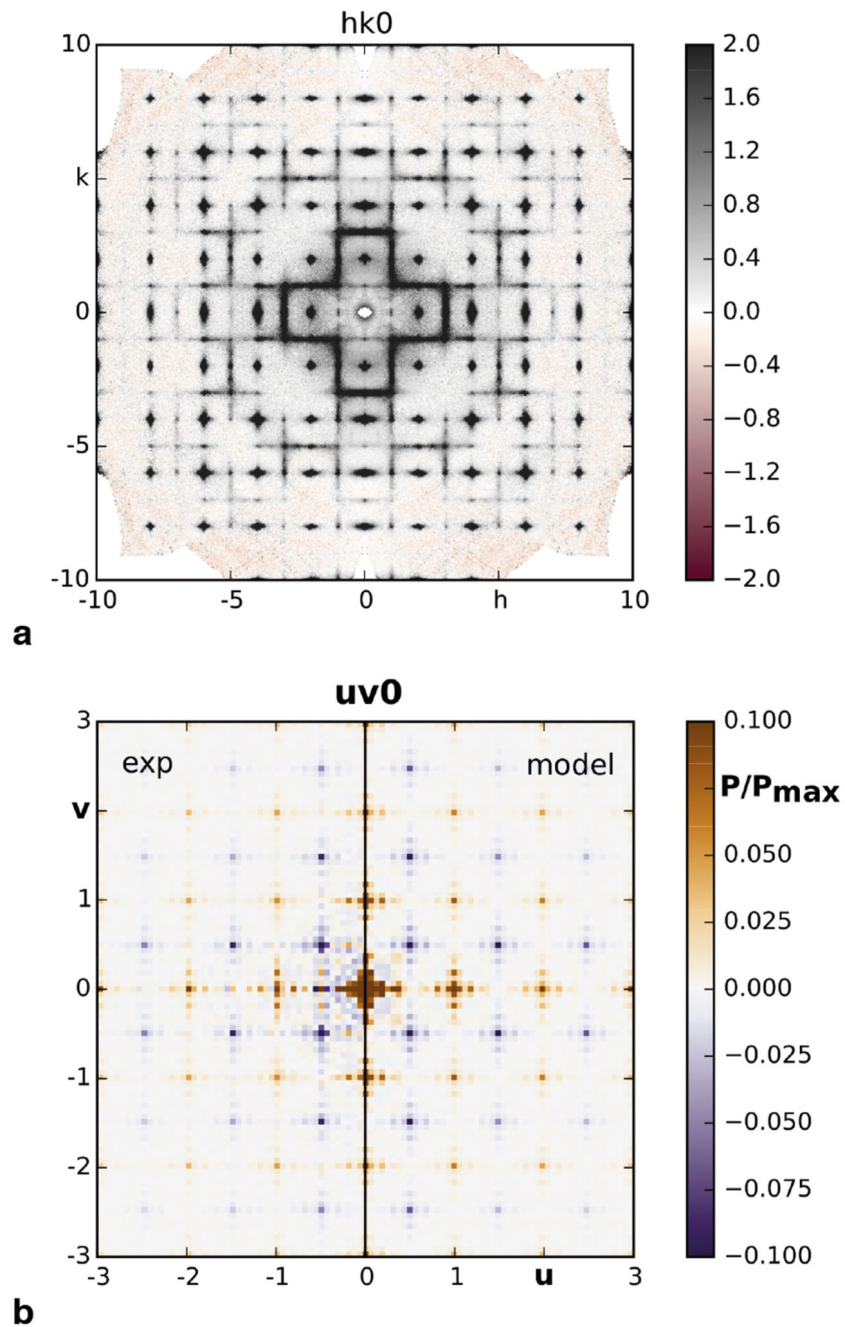
Extended Data
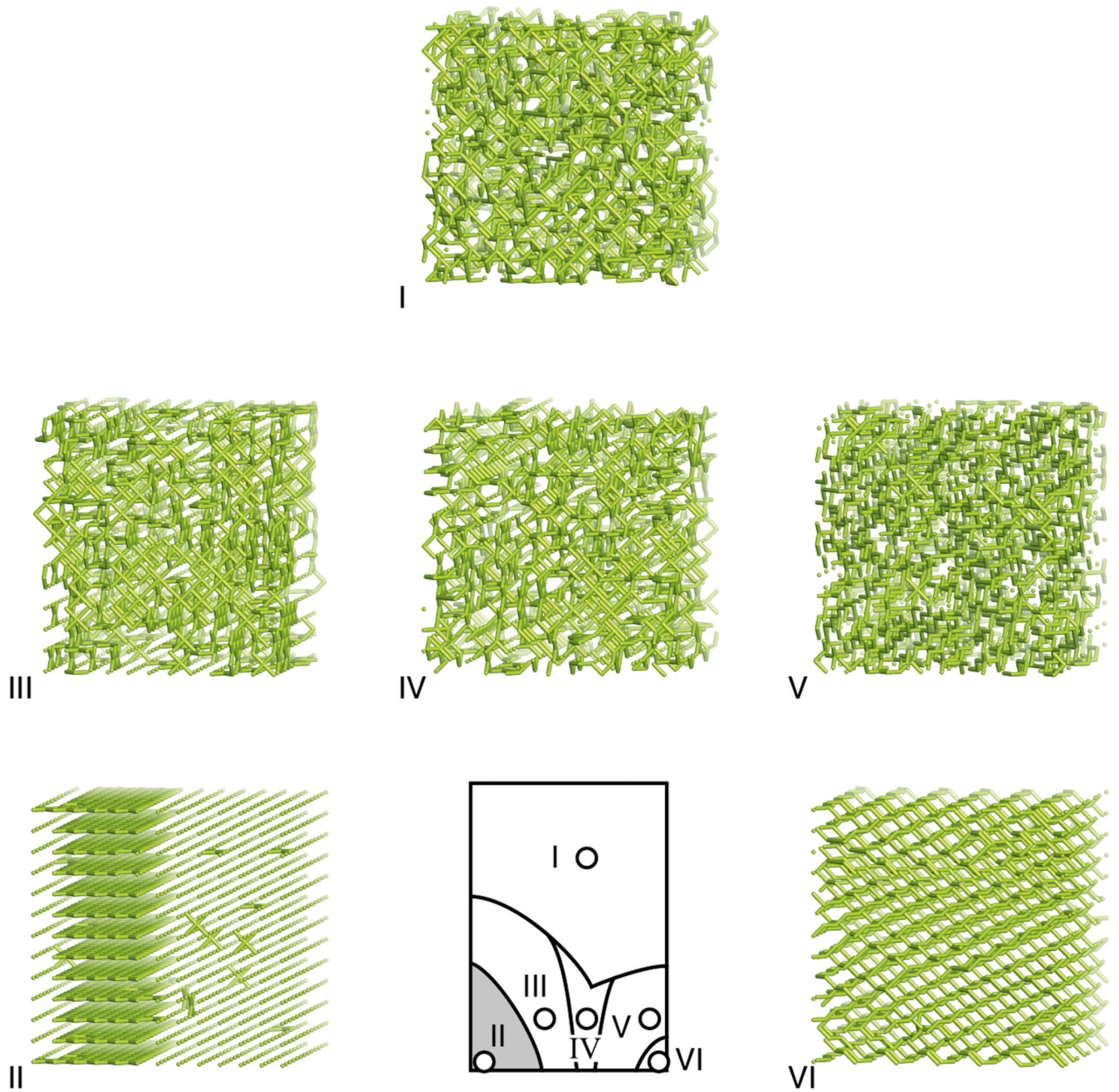
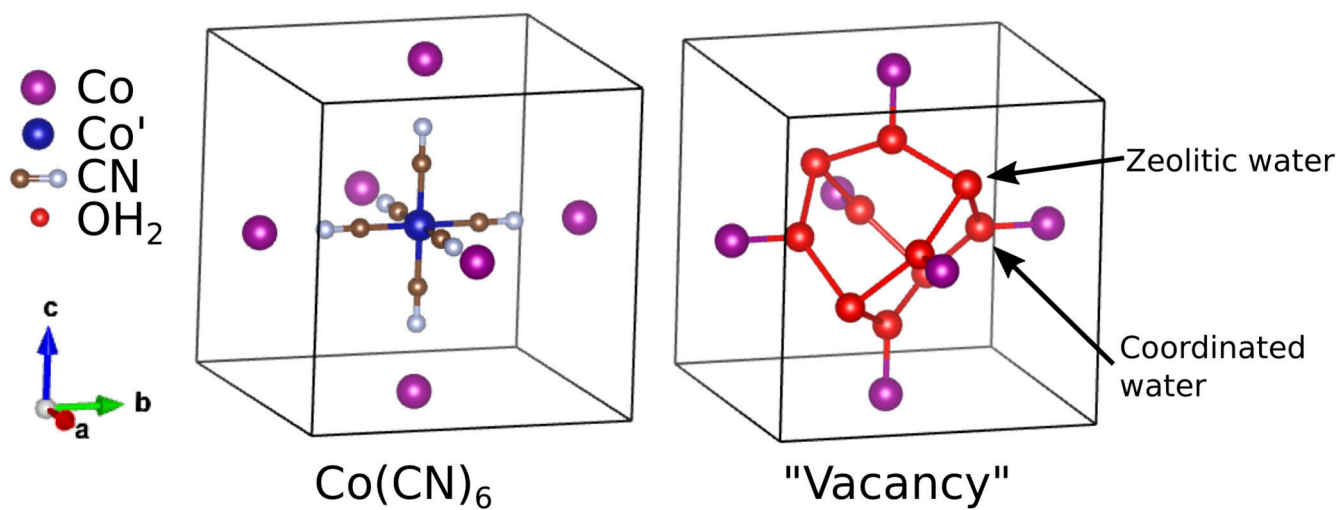**Extended data figure 1. Representative pore networks.**
Representative pore networks for each phase within the MC simulated phase diagram.

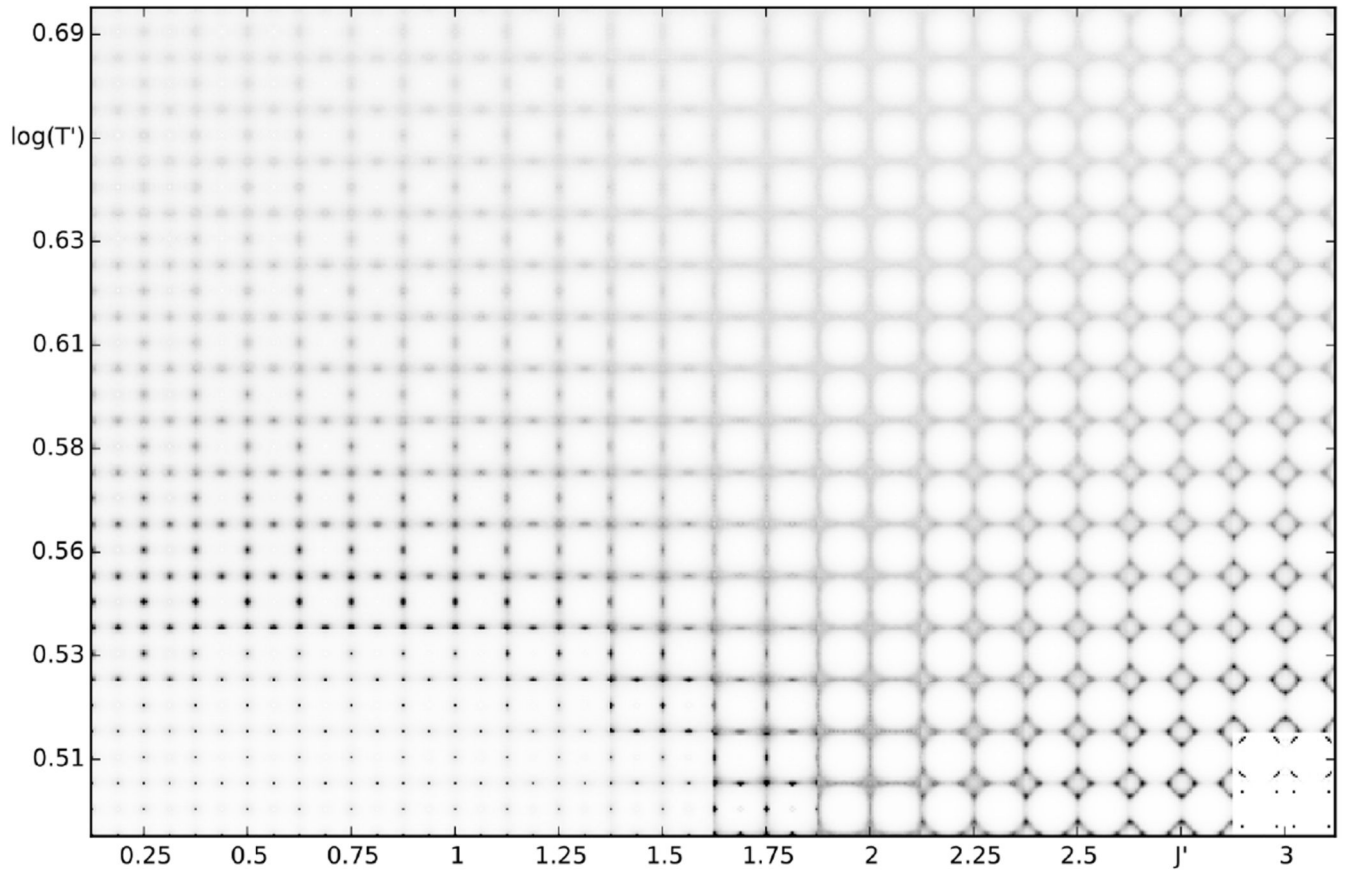**Extended data figure 2. Representative 3D- PDF.**
a Experimental diffuse scattering from the Co[Co] sample, *hk*0 section; **b** experimental and model 3D- PDF map of the Co[Co] sample, *uv*0 section.
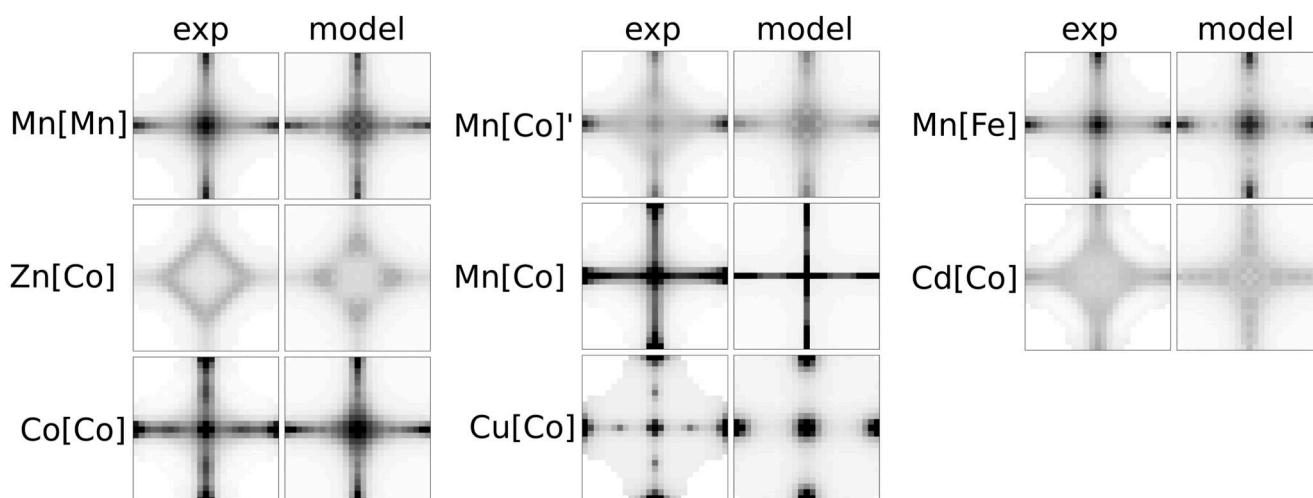
Extended data figure 3. M'-site models.
The structure of the $[Co(CN)_6]^{3-}$ and "vacancy" moieties used in our Co[Co] model.

Extended data figure 4. Alternative diffuse scattering phase map.
Diffuse scattering calculated with the modified model Hamiltonian (2).

Extended data figure 5. Diffuse scattering tiles.
Comparison of projected experimental diffuse scattering with the model diffuse scattering tiles for our various PBA samples; *cf* Figure 3.
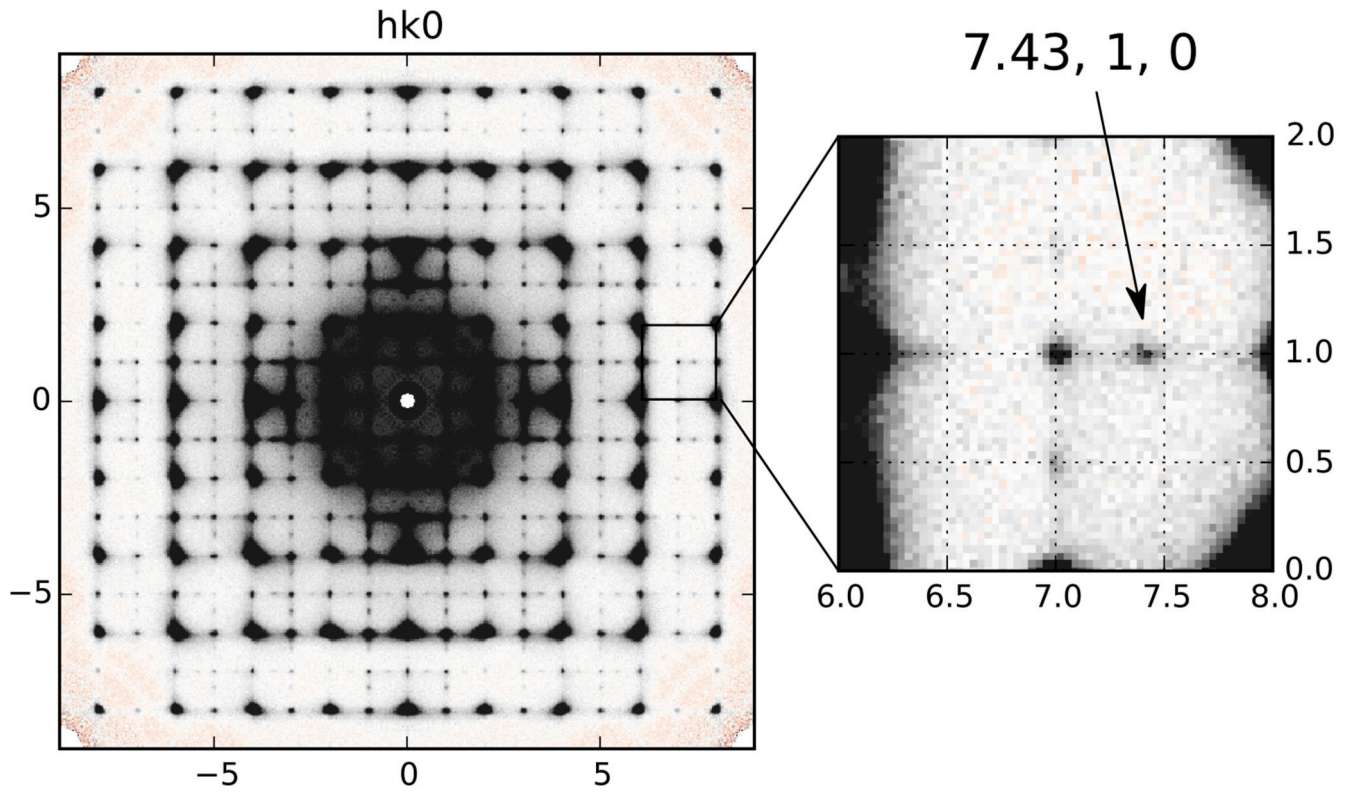
Extended data figure 6. Satellite reflections.
Satellite reflections in our Cu[Co] sample. The inset shows one specific satellite at (7.43, 1, 0).
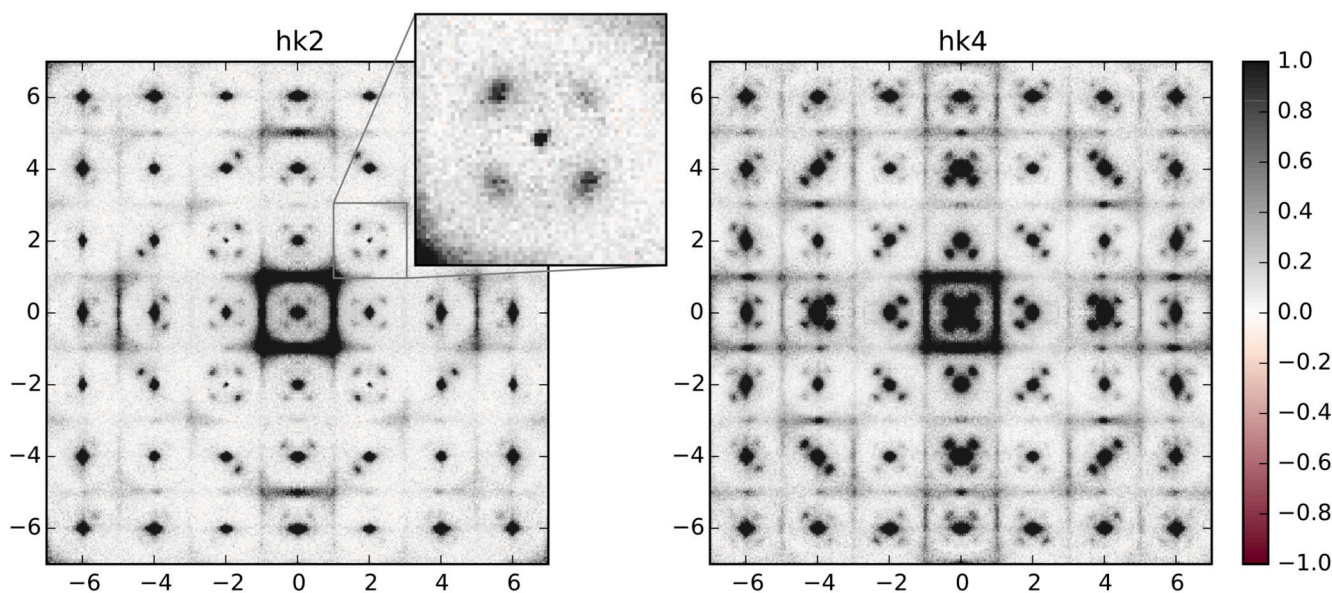
Extended data figure 7. Inelastic scattering.

Diffuse scattering in the Mn[Co]´ sample. Notice that the intensity of the diffuse scattering at $(h + 1/3, k + 1/3, l)$ positions increases with the increasing l: the scattering in the $hk4$ layer is stronger than in the $hk2$ layer.

Extended data table 1
Synthesis summary.

Precursor compositions and quantities used for PBA synthesis

PBA	Method	M^{2+} salt	n(M) (mmol)	K_3[M´(CN)$_6$]	n(M´) (mmol)
Cu[Co]	Gel	CuSO$_4$.5H$_2$O	0.03	K$_3$[Co(CN)$_6$]	0.02
Co[Co]	Gel	CoSO$_4$	0.30	K$_3$[Co(CN)$_6$]	0.20
Mn[Co]	Gel	MnSO$_4$.H$_2$O	0.12	K$_3$[Co(CN)$_6$]	0.12
Mn[Co]´	H-Cell	MnSO$_4$.H$_2$O	0.202	K$_3$[Co(CN)$_6$]	0.134
Mn[Fe]	H-Cell	MnSO$_4$.H$_2$O	0.131	K$_3$[Fe(CN)$_6$]	0.131
Cd[Co]	H-Cell	Cd(CH$_3$COO)$_2$	0.156	K$_3$[Co(CN)$_6$]	0.104
Zn[Co]	H-Cell	Zn(NO$_3$)$_2$.6H$_2$O	0.10	K$_3$[Co(CN)$_6$]	0.067

Extended data table 2
Data collection strategies.

Single-crystal X-ray diffuse scattering data collection strategies. Included in the last row are, for comparison, the relevant values for the Mn[Mn] sample reported in Ref. 31

PBA	Beamline	λ (Å)	r (Å)	Oscillation range (°)	ϕ (°)
Cu[Co]	I19	0.6889	0.83	360	0.1
Co[Co]	I19	0.6889	0.83	360	0.1

PBA	Beamline	λ (Å)	r (Å)	Oscillation range (°)	ϕ (°)
Mn[Co]	119	0.6889	0.83	360	0.1
Mn[Co]´	I19	0.6889	0.83	360	0.1
Mn[Fe]	I19	0.6889	0.83	360	0.1
Cd[Co]	BM01	0.6975	0.64	360	0.1
Zn[Co]	I19	0.6889	0.83	360	0.1
Mn[Mn]	BM01 (Mar345)	0.71	1.3	180	0.5

Extended data table 3

3D- PDF model.

Refined 3D- PDF correlation coefficients c of the first 44 neighbours.

u	*v*	*w*	*c*	*u*	*v*	*w*	*c*	*u*	*v*	*w*	*c*	*u*	*v*	*w*	*c*
0	0	0	1	0.5	1.5	2.5	-0.013	0.5	1.5	3	0.00065	1	3	3	0.002
0	0	1	0.15	0.5	2	2	0.019	0.5	2	2.5	-0.0025	1.5	1.5	2	-0.0034
0	0	2	0.071	0.5	2	3	0.014	0.5	2.5	3	-0.0012	1.5	1.5	3	-0.0012
0	0	3	0.047	0.5	2.5	2.5	-0.0097	1	1	1	-0.0057	1.5	2	2.5	-0.0025
0	0.5	0.5	-0.073	0.5	3	3	0.01	1	1	2	0.0033	1.5	2.5	3	-0.00025
0	0.5	1.5	-0.047	1	1	1	0.0056	1	1	3	0.0015	2	2	2	0.0051
0	0.5	2.5	-0.028	1	1.5	2	0.0078	1	1.5	2	0.0038	2	2	3	0.0047
0	1	1	0.033	1	1.5	3	0.0074	1	1.5	2.5	0.0002	2	2.5	2.5	-0.0012
0	1	2	0.025	1	2	1.5	-0.0025	1	2	2	0.0047	2	3	3	0.0033
0	1	3	0.018	1	2	2.5	-0.0043	1	2	3	0.0033	2.5	2.5	3	-0.0012
0	1.5	1.5	-0.021	1	2.5	2	-0.0012	1	2.5	2.5	-0.0007	3	3	3	-0.003

Supplementary Material

Refer to Web version on PubMed Central for supplementary material.

Acknowledgements

References

1. Kaye SS, Long JR. Hydrogen storage in the dehydrated Prussian blue analogues $M_3[Co(CN)_6]_2$ (M = Mn, Fe, Co, Ni, Cu, Zn). J Am Chem Soc. 2005; 127:6506–6507. [PubMed: 15869251]

2. Haas PA. A review of information on ferrocyanide solids for removal of cesium from solutions. Sep Sci Technol. 1993; 28:2479–2506.

3. Ohkoshi S-I, Nakagawa K, Tomono K, Imoto K, Tsunobuchi Y, Tokoro H. High proton conductivity in Prussian blue analogues and the interference effect by magnetic ordering. J Am Chem Soc. 2010; 132:6620–6621. [PubMed: 20420388]

4. Ferlay S, Mallah T, Ouahès R, Veillet P, Verdaguer M. A room-temperature organometallic magnet based on Prussian blue. Nature. 1995; 378:701–703.

5. Maurin I, Chernyshov D, Varret F, Blezen A, Tokoro H, Hashimoto K, Ohkoshi S-I. Evidence for complex multistability in photomagnetic cobalt hexacyanoferrates from combined magnetic and synchrotron x-ray diffraction measurements. Phys Rev B. 2009; 79

6. Rykov AI, Li X, Wang J. Crystal structure refinement of the electron-transfer-active potassium manganese hexacyanoferrates and isomorphous potassium manganese hexacyanocobaltates. J Solid State Chem. 2015; 227:35–44.

7. Bleuzen A, Lomenech C, Escax V, Villain F, Varret F, Cartier dit Moulin C, Verdaguer M. Photoinduced ferrimagnetic systems in Prussian blue analogues $C^I_xCo_4[Fe(CN)_6]_y$ (C^I = alkali cation). 1. Conditions to observe the phenomenon. J Am Chem Soc. 2000; 122:6648–6652.

8. Le-Khac, B; Chester, W. Highly active double metal cyanide catalysts. U.S. Patent 5,714,428. 1998.

9. Peeters A, Valvekens P, Ameloot R, Sankar G, Kirschhock CEA, De Vos DE. Zn–Co double metal cyanides as heterogeneous catalysts for hydroamination: A structure–activity relationship. ACS Catal. 2013; 3:597–607.

10. Wessells CD, Huggins RA, Cui Y. Copper hexacyanoferrate battery electrodes with long cycle life and high power. Nature Commun. 2011; 2:550. [PubMed: 22109524]

11. Pasta M, Wessells CD, Liu N, Nelson J, McDowell MT, Huggins RA, Toney MF, Cui Y. Full open-framework batteries for stationary energy storage. Nature Commun. 2014; 5:3007. [PubMed: 24389854]

12. Ludi A, Güdel H-U, Ruegg M. The structural chemistry of Prussian blue analogs. A single-crystal study of manganese(II)hexacyanocobaltate(III), $Mn_3[Co(CN)_6]_2 \cdot x H_2O$. Inorg Chem. 1970; 9:2224–2227.

13. Roque J, Reguerra E, Balmasseda J, Rodríguez-Hernández J, Reguera L, del Castillo LF. Porous hexacyanocobaltates(III): Role of the metal on the framework properties. Micro Meso Mater. 2007; 103:57–71.

14. Moritomo Y, Igarashi K, Kim J, Tanaka H. Size dependent cation channel in nanoporous Prussian blue lattice. Appl Phys Exp. 2009; 2

15. Xiong Q, Baychev TG, Jivkov AP. Review of pore network modelling of porous media: Experimental characteristics, network constructions and applications to reactive transport. J Contam Hydr. 2016; 192:101–117.

16. Grandjean F, Samain L, Long GJ. Characterization and utilization of Prussian blue and its pigments. Dalton Trans. 2016; 45:18018–18044. [PubMed: 27801448]

17. Keggin JF, Miles FD. Structures and formulæ of the Prussian blues and related compounds. Nature. 1936; 137:577–578.

18. Buser HJ, Schwarzenbach D, Petter W, Ludi A. The crystal structure of Prussian blue: $Fe_4[Fe(CN)_6]_3 \cdot xH_2O$. Inorg Chem. 1977; 16:2704–2710.

19. Herren F, Fischer P, Ludi A, Hälg W. Neutron diffraction study of Prussian blue, $Fe_4[Fe(CN)_6]_3 \cdot xH_2O$. Location of water molecules and long-range magnetic order. Inorg Chem. 1980; 19:956–959.

20. Sharpe, AG. The Chemistry of Cyano Complexes of the Transition Metals. Academic Press; London: 1976.

21. Buser H-J, Ron G, Ludi A, Engel P. Crystal structure of cadmium dhexacyanopalladate(IV). J Chem Soc, Dalton Trans. 1974:2473–2474.

22. Frisch JL. Notitia cœrulei Berolinensis nuper inventi. Misc Berolin. 1710; 1:377–378.

23. Chadwick BM, Sharpe AG. Transition metal cyanides and their complexes. Adv Inorg Chem Radiochem. 1966; 8:83–176.

24. Krap CP, Balmaseda J, del Castillo LF, Zamora B, Reguera E. Hydrogen storage in Prussian blue analogues: H_2 interaction with the metal found at the cavity surface. Energy Fuels. 2010; 24:581–589.

25. van der Marck SC. Calculation of percolation thresholds in high dimensions for FCC, BCC and diamond lattices. Int J Mod Phys C. 1998; 9:529–540.

26. Kaye SS, Long JR. The role of vacancies in the hydrogen storage properties of Prussian blue analogues. Catal Today. 2007; 120:311–316.

27. Roque-Malherbe R, Lugo F, Polanco R. Synthesis, structural elucidation and carbon dioxide adsorption on Zn(II) hexacyanoferrate(II) Prussian blue analogue. Appl Surf Sci. 2016; 386:360–367.

28. Flambard A, Köhler FH, Lescouëzec R. Revisiting Prussian blue analogues with solid-state MAS NMR spectroscopy: Spin density and local structure in $[Cd_3\{Fe(CN)_6\}_2] \cdot 15H_2O$. Angew Chem Int Ed. 2009; 48:1673–1676.

29. Calderon HA, Reguera E. HREM of porous Prussian blue type materials for hydrogen storage. Microsc Microanal. 2012; 18:1468–1469.

30. Franz P, Ambrus C, Hauser A, Chernyshov D, Hostettler M, Hauser J, Keller L, Krämer K, Stoeckli-Evans H, Pattison P, Bürgi H-B, et al. Crystalline, mixed-valence manganese analogue of Prussian blue: Magnetic, spectroscopic, X-ray and neutron diffraction studies. J Am Chem Soc. 2004; 126:16472–16477. [PubMed: 15600350]

31. Chernyshov D, Bosak A. Diffuse scattering and correlated disorder in manganese analogue of Prussian blue. Phase Trans. 2010; 83:115–122.

32. Welberry TR, Weber T. One hundred years of diffuse scattering. Cryst Rev. 2016; 22:2–78.

33. Weber T, Simonov A. The three-dimensional pair distribution function analysis of disordered single crystals: basic concepts. Z Krist. 2012; 227:238–247.

34. Pauling, L. The Nature of the Chemical Bond and the Structure of Molecules and Crystals: An Introduction to Modern Structural Chemistry. Cornell University Press; Ithaca NY: 1960.

35. Paciak M, Welberry TR, Kulda J, Kempa M, Hlinka J. Polar nanoregions and diffuse scattering in the relaxor ferroelectric $PbMg_{1/3}Nb_{2/3}O_3$. Phys Rev B. 2012; 85

36. Battle PD, Evers SI, Hunter EC, Westwood M. $La_3Ni_2SbO_9$: A relaxor ferromagnet. Inorg Chem. 2013; 52:6648–6653. [PubMed: 23688332]

37. Zhadanov H. Crystalline structure of $Zn(CN)_2$. C R Acad Sci URSS. 1941; 31:352–354.

38. Shugam E, Zhdanov H. The crystal structure of cyanides. The structure of $Cd(CN)_2$. Acta Physiochim URSS. 1945; 20:247–252.

39. Siebert H, Jentsch W. Rhomboedrisch kristallisierende Zink-hexacyanometallate(III) $Zn_3[M(CN)_6]_2$. Z Naturforsch. 1981; 36b:123–124.

40. Bear, J. Dynamics of Fluids in Porous Media. Dover; New York: 1988.

41. van der Linden JH, Narsillo GA, Tordesillas A. Machine learning framework for analysis of transport through complex networks in porous, granular media: A focus on permeability. Phys Rev E. 2016; 94

42. Epstein N. On tortuosity and the tortuosity factor in flow and diffusion through porous media. Chem Eng Sci. 1989; 44:777–779.

43. Fang Z, Bueken B, De Vos DE, Fischer RA. Defect-engineered metal–organic frameworks. Angew Chem Int Ed. 2015; 54:7234–7254.

44. Zhang T, Jin S, Gu Y, He Y, Li M, Li Y, Fan H. SFX analysis of non-biological polycrystalline samples. IUCrJ. 2015; 2:322–326.

45. Yun Y, Zou X, Hovmöller S, Wan W. Three-dimensional electron diffraction as a complementary technique to powder X-ray diffraction for phase identification and structure solution of powders. IUCrJ. 2015; 2:267–282.

46. Chapman KW, Chupas PJ, Maxey ER, Richardson JW. Direct observation of adsorbed H_2-framework interactions in the Prussian blue analogue $Mn^{II}_3[Co^{III}(CN)_6]_2$: The relative importance of accessible coordination sites and van der Waals interactions. Chem Commun. 2006:4013–4015.

47. Ojwang DO, Grins J, Wardecki D, Valvo M, Renman V, Häggström L, Ericsson T, Gustafsson T, Mahmoud A, Hermann RP, Svensson G. Structure characterization and properties of K-containing copper hexacyanoferrate. Inorg Chem. 2016; 55:5924–2934. [PubMed: 27258790]

48. Liu L, Chen Z, Wang J, Zhang D, Zhu Y, Ling S, Huang K-W, Belmabkhout Y, Adil K, Zhang Y, Slater B, et al. Imaging defects and their evolution in a metal–organic framework at sub-unit-cell resolution. Nature Chem. 2019; 11:622–628. [PubMed: 31086300]

49. Brunklaus G, Koller H, Zones SI. Defect models of as-made high-silica zeolites: Clusters of hydrogen-bonds and their interaction with the organic structure-directing agents determined from ^{1}H double and triple quantum NMR spectroscopy. Angew Chem Int Ed. 2016; 55:14459–14463.

50. Jaffe B, Roth RS, Marzullo S. Piezoelectric properties of lead zirconate-lead titanate solid-solution ceramics. J Appl Phys. 1954; 25:809–810.

51. Kabsch W. XDS. Acta Cryst D. 2010; 66:125–132. [PubMed: 20124692]

52. Logvinovich D, Simonov A. MEERKAT.

53. Schmidt E, Neder RB. Diffuse single-crystal scattering corrected for molecular form factor effects. Acta Cryst A. 2017; 73:231–237.

54. Simonov A, Weber T, Steurer W. Experimental uncertainties of three-dimensional pair distribution function investigations exemplified on the diffuse scattering from a tris-*tert*-butyl-1,3,5-benzene tricarboxamide single crystal. J Appl Cryst. 2014; 47:2011–2018.

55. Blessing RH. Outlier treatment in data merging. J Appl Cryst. 1997; 30:421–426.

56. Kobas M, Weber T, Steurer W. Structural disorder in the decagonal Al–Co–Ni. I. Patterson analysis of diffuse x-ray scattering data. Phys Rev B. 2005; 71

57. Simonov A, Weber T, Steurer W. *Yell*: a computer program for diffuse scattering analysis *via* three-dimensional delta pair distribution function refinement. J Appl Cryst. 2014; 47:1146–1152.

58. Earl DJ, Deem MW. Parallel tempering: Theory, applications, and new perspectives. Phys Chem Chem Phys. 2005; 7:3910–3916. [PubMed: 19810318]

59. Welberry TR, Goossens DJ, Edwards AJ, David WIF. Diffuse X-ray scattering from benzil, $C_{14}H_{10}O_2$: analysis *via* automatic refinement of a Monte Carlo model. Acta Cryst A. 2001; 57:101–109. [PubMed: 11124508]

60. Willems TF, Rycroft CH, Kazi M, Meza JC, Haranczyk M. Algorithms and tools for high-throughput geometry-based analysis of crystalline porous materials. Micro Meso Mater. 2012; 149:134–141.

61. Aschauer U, Spaldin NA. Interplay between strain, defect charge state, and functionality in complex oxides. Appl Phys Lett. 2016; 109
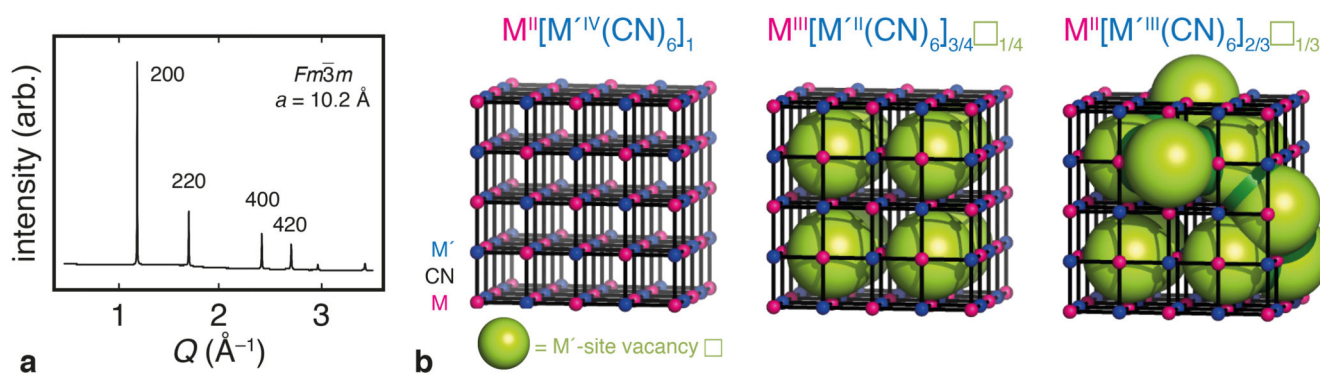
Figure 1. Structure of PBAs.

a X-ray powder diffraction pattern of Mn[Co], which is typical for PBAs. **b** The parent structure type (left) comprises interpenetrating FCC arrays of M and M′ cations (pink and blue spheres, respectively), bridged by cyanide ions (black rods). In Prussian blue (centre), ¼ of the M′ sites are vacant, creating isolated micropores (green spheres) that are usually occupied by water. In PBAs, $\frac{1}{3}$ of M′ sites are vacant. There are now sufficiently many vacancies that neighbouring pores must connect (dark green collars) to give an extended micropore network. The characteristics of this network depend on vacancy correlations.
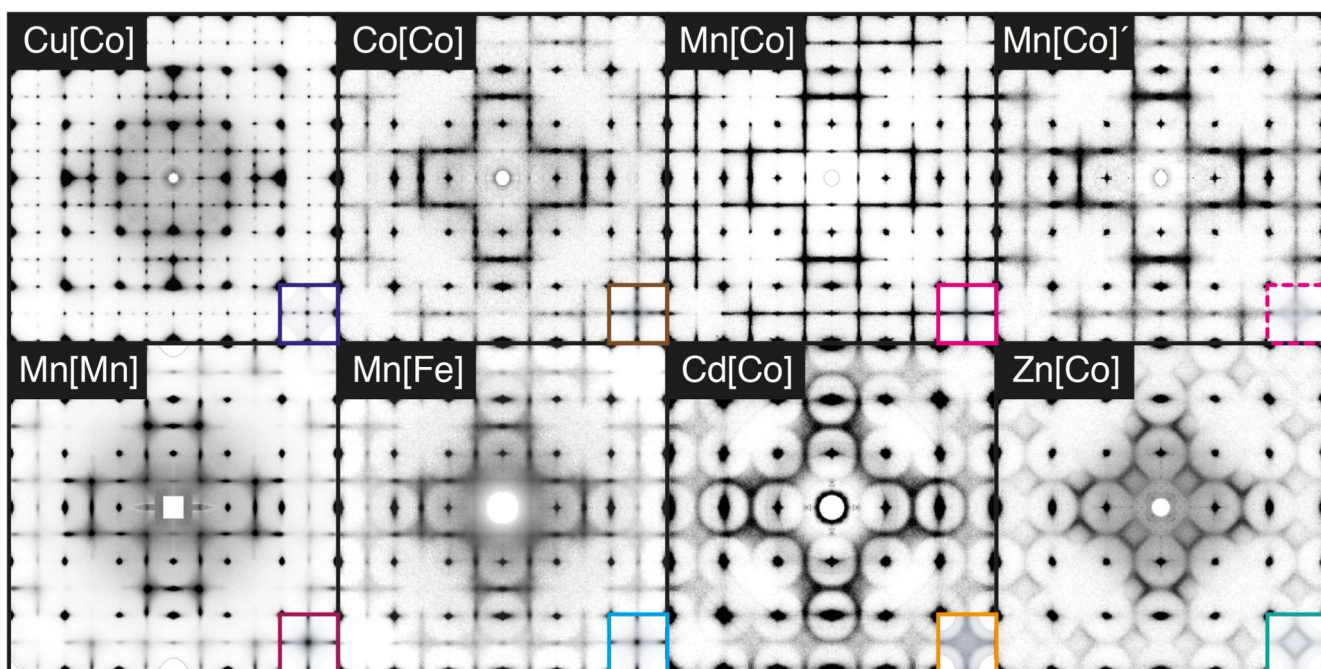
Figure 2. Single-crystal diffuse scattering from PBAs.
Reconstructed ($hk0$) scattering planes are shown here for eight PBA samples ($-6 < |h|,|k| <$ 6). The data for Mn[Mn] are those reported in Ref. 31. At the bottom-right corner of each panel is the diffuse scattering pattern averaged over all squares with δh, $\delta k = 2$ in the ($hk0$) scattering plane. Intensities near the Bragg positions with even h,k in the corners of the squares have been removed. Note the fundamental difference in information content of these single-crystal data relative to PXRD traces of the same materials [cf. Figure 1a].
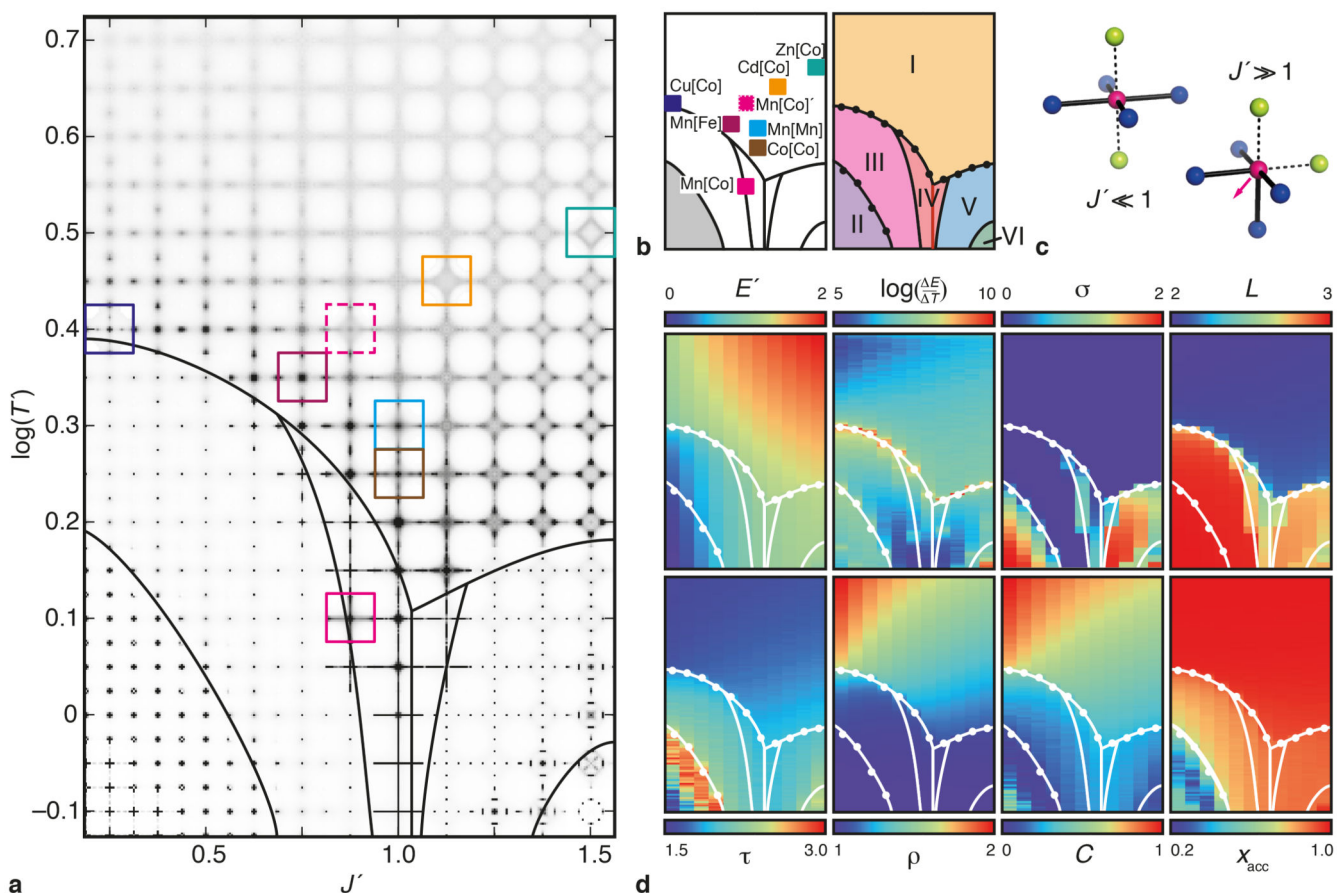
Figure 3. Vacancy network phase diagram.
a MC diffuse scattering map with experimental plane-averaged scattering superimposed (squares). **b** Distribution of PBAs (left) and vacancy polymorphs (I–VI) demarcated by MC specific heat anomalies (white circles) and a morphotropic phase boundary (red line).[50] Lines are guides to the eye. **c** Centrosymmetric and pseudotetrahedral M-site geometries. **d** Thermodynamic and micropore network characteristics: normalised MC energy E'; MC energy gradient $\log\left(\frac{\Delta E}{\Delta T}\right)$; anisotropy $\sigma = \Sigma(I - \hat{I})^2$, where I and $\hat{I}$ are the diffuse scattering intensities before and after Laue symmetrisation; scattering localisation $L = \log\left[\frac{\Sigma I^2}{(\Sigma I)^2}\right]$; surface-accessible vacancy fraction x_{acc}; conductance C; vacancy-neighbour pairs per formula unit ρ; and tortuosity τ.
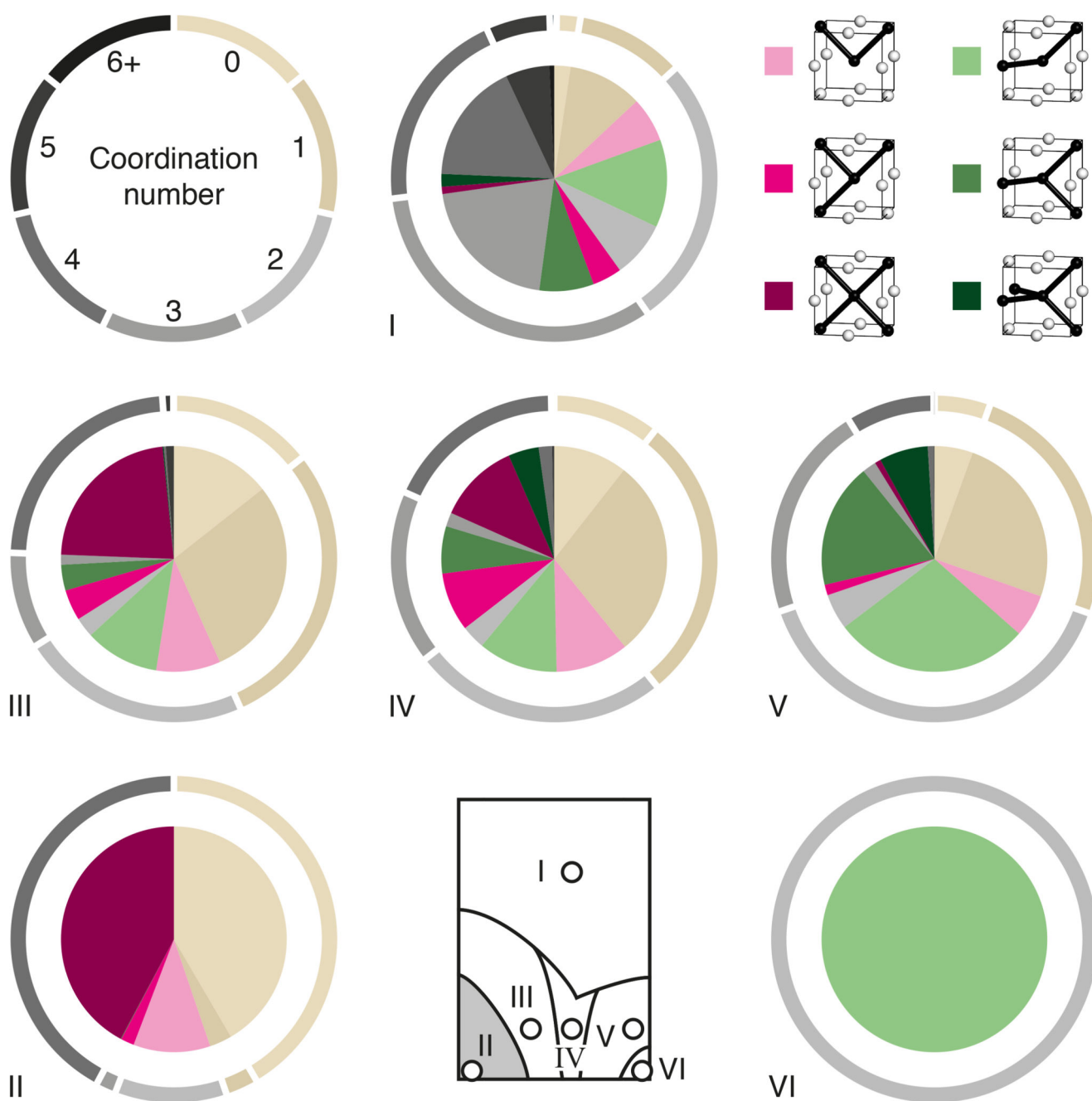
Figure 4. Statistical properties of micropore networks.
Network coordination number and geometry distributions are given as interior and exterior pie charts, respectively. For each coordination number 2, coordination geometries related to square-planar networks are shaded pink; those related to tetrahedral networks are shaded green; all others are collated for a given coordination number and shaded in grey. Coordination geometries are given at the top right: empty and filled circles denote occupied

and vacant M′-sites, respectively, and bold lines show connected channels. Note the general preference for 90° pore angles at low J' and 120° angles at high J'.